Coupling of Acetaldehyde to Crotonaldehyde on CeO_{2-x}(111): Bifunctional Mechanism and Role of Oxygen Vacancies

Journal:	*The Journal of Physical Chemistry*
Manuscript ID	jp-2018-085357.R1
Manuscript Type:	Special Issue Article
Date Submitted by the Author:	n/a
Complete List of Authors:	Zhao, Chuanlin; Louisiana State University, Department of Chemical Engineering Watt, Charles; Princeton University; Oak Ridge National Laboratory Kent, Paul; Oak Ridge National Laboratory, Center for Nanophase Materials Sciences Overbury, Steven; Oak Ridge National Laboratory Mullins, David; Oak Ridge National Laboratory, Calaza, Florencia; INTEC (CONICET-UNL), Savara, Aditya; Oak Ridge National Laboratory, Chemical Sciences Division Xu, Ye; Louisiana State University, Department of Chemical Engineering

Coupling of Acetaldehyde to Crotonaldehyde on $CeO_{2-x}(111)$: Bifunctional Mechanism And Role of Oxygen Vacancies

Chuanlin Zhao[†], Charles Watt[‡#], Paul R. Kent[§], Steven H. Overbury[‡], David R. Mullins[‡], Florencia C. Calaza[¶], Aditya Savara[*‡], Ye Xu[*†]*

[†] Cain Department of Chemical Engineering, Louisiana State University, Baton Rouge, LA 70803, USA

[‡] Chemical Sciences Division, Oak Ridge National Laboratory, Oak Ridge, TN 37831, USA

[#] Princeton University, Princeton, NJ 08544, USA

[§] Center for Nanophase Materials Sciences, Oak Ridge National Laboratory, Oak Ridge, TN 37831, USA

[¶] Instituto de Desarrollo Tecnológico para la Industria Química (INTEC) CONICET – UNL, Santa Fe (3000), Argentina

* Corresponding Authors. Email addresses: fcalaza@intec.unl.edu.ar (F. Calaza); savaraa@ornl.gov (A. Savara); yexu@lsu.edu (Y. Xu).

Abstract

Selective C-C coupling of oxygenates is pertinent to the manufacture of fuel and chemical products from biomass and from derivatives of C_1 compounds (i.e., oxygenates produced from methane and CO_2). Here we report a combined experimental and theoretical study on the temperature-programmed reaction (TPR) of acetaldehyde (AcH) on a partially reduced CeO_{2-x}(111) thin film surface. The experiments have been carried out under ultra-high vacuum conditions without continuous gas exposure, allowing better isolation of active sites and reactive intermediates than in flow reactor conditions. AcH does not undergo aldol condensation in a typical TPR procedure, even though the enolate form of AcH (CH_2CHO) is readily produced on CeO_{2-x}(111) with oxygen vacancies. We find however that a tailored "double-ramp" TPR procedure is able to successfully produce an aldol adduct, crotonaldehyde (CrA). Using density functional theory calculations and microkinetic modeling we explore several possible C-C coupling pathways. We conclude that the double-ramp procedure allows surface oxygen vacancy dimers, stabilized by adsorbate occupation, to form dynamically during the TPR. The vacancy dimers in turn enable C-C coupling to occur between an enolate and an adjacent AcH molecule via a ~~bifunctional~~ enolate-keto ~~cation~~ mechanism that is distinct from conventional acid- or base-catalyzed aldol condensation reactions. The proposed mechanism indicates that CrA desorption is rate-limiting while C-C coupling is facile.

1. Introduction

Aldol condensation reactions are considered one of the key C-C bond forming reactions for biomass upgrading processes. Together with etherification, ketonization and esterification, they allow for the upgrading of bio-derived short-chain oxygenates to longer chains without a significant loss of C content in the final products.[1-2] Aldol condensation involves an addition reaction between two aldehyde or ketone molecules by forming a C-C bond with the release of a water molecule as a by-product, thus lowering the oxygen content in a longer chain product and increasing the total C/O ratio, relative to the reactants. This reaction to extend the carbon chain can be followed by hydrogenation if greater saturation is needed for heavier fuels or lubricants. Earlier, Huber et al.[3] reported the feasibility of producing liquid hydrocarbons from sugar feedstocks (cellulose, sorbitol, furfural and others) using a four-step process, in which a cross aldol reaction is the key step for C-C bond formation. While aldol condensation has been known and used for over a century, there are specific heterogeneously catalyzed reactions where the mechanism remains incompletely understood.

The commonly accepted mechanism for carbonyl compounds[4] depends on the environment in which the reaction occurs, and is generally described as catalyzed by either an acid or a base. This distinction is incomplete, in terms of possibilities, as will be discussed later, but we will introduce the topic in the common context. When aldol condensation is base-catalyzed, it has been proposed that an enolate intermediate is formed by dehydrogenation of an α–C of one of the aldehydes (forming a C=C-O moiety), which then attacks as a nucleophile a second aldehyde at the carbonyl C. In the case of a acid-catalyzed reaction mechanism, an enol intermediate is formed (C=C-OH) which then acts as a nucleophile which attacks a second carbonyl molecule that has been activated by coordination to the acid through the carbonyl oxygen. In

homogeneous catalytic reactions the mechanism is important in determining the stereo symmetry and regioselectivity of the final product. For heterogeneous catalytic reactions the nature and spatial distribution of active sites on the solid surface may change the preferred mechanism. Historically, aldol reactions have been studied on solid materials classified as either acidic or basic. Basic oxides were thought to favor the formation of enolate intermediates, as in the case of acetone aldol condensation on MgO,[5] where the rate-limiting step is the coupling of the enolate with acetone. For reducible oxides, which are amphoteric, experimental data have been interpreted as indicating that the dominant mechanism could change from a base mechanism to an acid mechanism.[6] With reducible oxides, the relative rate of the enolate formation and further insertion into the second carbonyl containing molecule is believed to be adjustable by varying the amount of Lewis and Brønsted acid sites available.[6] Therefore, it is normally understood that this reaction works best on a solid material that can act as a bifunctional catalyst that provides both acid and base sites.[7-8] In this context, referring to an aldol reaction on a reducible oxide as either acid-catalyzed or base-catalyzed is imprecise, and a more comprehensive terminology will be used in the Discussion section below.

On reducible oxides, the work by Idriss and Barteau[9-11] elucidated a wide variety of aspects regarding the mechanism and selectivity of aldol condensation reactions, including on CeO_2 and TiO_2. By varying the extent of reduction of TiO_2, it was found that the stoichiometric surface favored the aldol product while more reduced surfaces produced butene, and this result was hypothesized to be general to reducible oxides.[11] Idriss and Barteau interpreted the data as meaning that lattice oxygen atoms acted as bases to abstract the α hydrogen, which is consistent with interpretations of other studies on oxides.[5-7, 10-17] With this idea in mind, the aldol reaction was facilitated on acidic supports by the addition of basic promoters or modifiers (such that the

base could abstract the alpha hydrogen).[12, 14] Other studies on varying catalysts/supports and with varying the catalyst pre-treatments showed evidence that it is possible to functionalize catalyst surfaces with the right amount of acid-base site pairs needed for a specific reaction.[15-17]

In the last few years, an increased interest for aldol reactions has been seen in the literature, with more researchers following the idea of tailoring specific catalytic materials depending on the reaction under study.[18-20] Kinetic isotope labeling experiments have shown evidence for a bifunctional mechanism on TiO_2 where base sites are thought to abstract hydrogen to form enolates that then nucleophilically attack the carbonyl group of another molecule that is activated (made more reactive) by an acid site.[19] Bifunctional catalysts of various types have been proposed on theoretical or experimental grounds, and their intrinsic relationships with activity and selectivity measurements are being explored for the sake of further improving the chemical process.[19, 21-23] Wang and Iglesia have recently published a study on the activity of aldol reactions over TiO_2, building on the existing knowledge, and concluding that Lewis acid-base site pairs of modest acid–base strength and acid–base site distances are preferred for turning over aldol condensation.[21]

As a reducible oxide, CeO_2 provides an ideal platform on which to study aldol condensation reactions and to explore the effects of surface structure and vacancy formation on the reactions. It has been proven, first on model systems[24-26] and later on nanoparticles with characteristic shapes,[27] that when ceria is exposed to acetaldehyde (AcH), the interactions of the molecules with the surface depends strongly on the amount of vacancies in the surface. AcH adsorbs weakly on the stoichiometric (111) surface but interacts strongly in the presence of vacancies, as made evident by temperature programmed desorption of AcH from model CeO_2(111) surfaces. In the latter case, AcH can form an enolate species by dehydrogenating the CH_3 moiety at the α-

C.[26] The existence of the enolate of AcH has been confirmed by reflection-absorption infrared spectroscopy (RAIRS), and by density functional theory (DFT) based simulated infrared spectra and microkinetic modeling, to be the dominant species between approximately 400 and 600 K.[26, 28] The formation of the reductive C_2 products is well understood,[28] but a major challenge in understanding is presented by the C_4 products that result from C-C coupling: Such molecules are among the prevalent products in the reactor study using CeO_2 nanoparticles,[27] but they do not appear in ultra-high vacuum (UHV) studies on fully oxidized and partially reduced CeO_2(111).[24, 26, 29]

In this study, we found a method to enhance C_4 products in a temperature-programmed ramp over CeO_{2-x}(111) by applying what we call a "double-ramp" temperature programmed reaction (TPR) procedure. This procedure gave additional control of the amount and distribution of the reaction intermediates and oxygen vacancies on model CeO_{2-x}(111) surfaces, thereby enabling the aldol condensation of acetaldehyde to crotonaldehyde (i.e., 2-butenal; abbreviated as CrA) under UHV conditions. Consistent with the new TPR procedure, we extended the reaction mechanism previously proposed for AcH TPR on CeO_{2-x}(111)[28] and investigated several reaction mechanisms to account for CrA formation, which were modeled using DFT calculations and mean-field microkinetic modeling. The overall results led us to conclude that oxygen vacancy dimers are required for the observed C-C coupling reaction. Therefore, the dynamic behavior of oxygen vacancies is an influential factor in ceria surface chemistry, which cannot be easily revealed without a combination of UHV experiments based on the special procedure that we have developed and first-principles-based theoretical and computational modeling.

2. Methods

2.1 Experimental

Experiments were performed at Oak Ridge National Laboratory (ORNL), as described previously.[26] The most pertinent details including deviations from our previous experiments are described here. The base pressure of the instrument is typically between 1×10^{-10} and 4×10^{-10} Torr. Fully oxidized CeO_2(111) films were grown *in situ* by Ce vapor deposition onto a Ru(0001) surface at 700 K with $>1\times10^{-7}$ Torr O_2 as described previously.[30] Partially reduced CeO_{2-x}(111) films were grown using lower oxygen pressures during deposition. The Ce oxidation state was determined using X-ray photoelectron spectroscopy (XPS) of the Ce 3d and Ce 4d regions at ORNL, as described previously.[31] It had been found that $\sim5\times10^{-8}$ Torr O_2 was suitable for growing the partially reduced films with oxygen vacancies where approximately 60% of the cerium was in the 3+ state according to XPS, which means the film was largely reduced and corresponds to a stoichiometry of $CeO_{1.70}$ at the surface (the maximum reduction would be 100% Ce^{3+} and correspond to a stoichiometry of $CeO_{1.5}$).

AcH was introduced using a cylindrical gas doser with a 10 μm diameter aperture. The adsorption of AcH was conducted at 160-175 K, which is more than 40 K above the nominal multilayer desorption temperature (~110 K) and ensured that one monolayer was present at the start of experiment. Subsequent to AcH adsorption, two types of temperature programmed reaction (TPR) experiments were performed. First, a conventional TPR was performed in which the temperature of the surface was subjected to a single temperature ramp. In separate experiments, a tailored temperature-controlled procedure was used in which the temperature ramp was broken and stopped at a set temperature, the sample was cooled to 160-175 K, and

then additional reactant (e.g. AcH) was introduced and a second temperature ramp was performed (see Results section for further description).

The TPR experiments were performed in an UHV chamber at ORNL. In all TPR experiments the temperature was ramped at 2 K/s. Gases evolved were monitored with a UTI 100-C mass spectrometer. The TPR occurred in a "line-of-sight" geometry with the sample facing the ionization region of the mass spectrometer and within several centimeters of it. The masses monitored during experiments to produce CrA were, in atomic mass units: 2, 18, 26, 27, 28, 29, 31, 39, 41, 44, 45, 56, 57, and 70. The signals were linear baseline corrected. The signals were then smoothed using boxcar linear regression, with each box smaller than the width of the peaks: The final TPR spectra were still not completely smooth, which is one indication that the data were not over-smoothed. The signals were first resolved with an in-house computer code, MSRESOLVE-SG, using a procedure called sequential linear subtraction. In sequential linear subtraction, one or more molecules' contributions to the observed mass spectrometry signals are resolved (attributed to a molecule) and then that molecule's (or molecules') contributions are subtracted across all masses, based on the reference pattern. The reference spectrum for AcH was obtained with the instrument used. For the other molecules, reference spectra were obtained from the electron ionization mass fragmentation spectra available at NIST WebBook,[32] with a mass-dependent tuning factor correction applied for our mass spectrometer based on the measured AcH spectrum. The final reference patterns used are included in the Supporting Information (Table S1). The signals that were able to be resolved, in terms of molecules and mass to charge ratios, are: hydrogen: 2, crotonaldehyde: 70, crotyl alcohol: 57, acetaldehyde: 41, ethanol: 31, water: 18, carbon dioxide: 44, ethylene and acetylene: 26 and 27, and carbon monoxide: 28. These molecules, with this set of masses, were able to be resolved using

sequential linear subtraction: At each step, the molecule being solved for had one or more mass fragments that were unique relative to the remaining molecules. The resolved signals were then converted to resolved molecular concentrations (in arbitrary units, but on a common scale) based on correction factors determined using the method of Madix and Ko.[33] These resolved molecular concentrations represented the relative gas phase concentrations of the molecules based on the signals detected by the mass spectrometer, and are plotted in Figures 1 and 2 below.

2.2 Computational

Periodic, spin-polarized DFT calculations were performed using the Vienna Ab initio Simulation Package (VASP).[34] The generalized gradient approximation (GGA-PW91)[35] was used consistent with our previous studies.[26, 28, 36] The optB86b van der Waals (vdW) functional[37-38] was used to estimate the vdW contribution in the adsorption of AcH and CrA. The core electrons were described using projector-augmented wave (PAW) method,[39] and the Kohn-Sham valence states [Ce(5s5p4f5d6s), O(2s2p), C(2s2p), H(1s)] were expanded in a plane wave basis set with 400 eV kinetic energy cutoff.

The DFT+U formalism of Dudarev et al. was used to partially offset the 4f electron delocalization error in DFT at the GGA level.[40-41] A U value of 2 eV was used based on our previous studies,[26, 28, 36] with a U value of 5 eV used in limited cases for comparison. Larger U values produce better predictions for electronic structures[42] but less accurate predictions of temperature-programmed reaction kinetics in terms of peak desorption temperatures.[26] Small U values ($\leq$ 2 eV) have also been recommended based on comparison with experimental reaction[42-43] and adsorption[44] energies. The equilibrium lattice constant of the CeO_2 bulk was calculated to

be 5.476 and 5.494 Å (U= 2 and 5 eV, respectively) on a (15×15×15) MP k-point grid, in close agreement with previous studies.[45]

Each slab model for the CeO_2(111) surface consisted of three O-Ce-O tri-layers, with the top tri-layer fully relaxed and the remaining two tri-layers fixed at the bulk positions. The slab was separated from its periodic images in the *z* direction by ~12 Å of vacuum. Adsorption was studied only on one side of the slab (adsorbates are fully relaxed), with dipole decoupling applied in the z direction.[46] The adsorption energy was calculated as $\Delta E_{ads} = E_{total} - E_{slab} - E_{gas}$, where E_{total}, E_{slab}, and E_{gas} refer to the energy of the slab with the adsorbate, the energy of the clean surface, and the energy of gas-phase adsorbate in a neutral state, respectively. The trans isomer of CrA was used throughout this study because it is calculated to be 0.12 eV more stable in the gas phase than the cis isomer and because the latter causes additional unfavorable steric interactions when adsorbed on the surface.

The minimum energy reaction path for each proposed elementary step and its transition state (TS) were determined using the climbing-image nudged elastic band method and dimer method.[47-50] The activation energy was calculated as $E_a = E_{TS} - E_{IS}$, where E_{TS} and E_{IS} refer to the energy of the transition state and corresponding initial state, respectively. The corresponding reaction energy of an elementary step is $\Delta E_{rxn} = E_{FS} - E_{IS}$. Convergence criteria for both geometry optimization and transition state search were set to the extent that the maximum residual force was 0.01 eV/Å or less in all relaxed degrees of freedom. The singlet-triplet/doublet-quadruplet splitting was checked, and the lower adsorption energy for an adsorbate and the lower activation energy for a given elementary step are reported below. Transition states were verified to possess only one vibrational mode with a negative curvature that in the direction of the bond breaking of forming process. Vibrational modes and frequencies

were calculated using a finite difference approximation approach of the dynamical matrix with a displacement of 0.01 eV/Å. If not specified, the ΔE_{ads}, E_a, and ΔE_{rxn} values were calculated on p(2×2) surface unit cells. The values reported in the main text are based on DFT total energies only, while zero-point energy (ZPE) and free energy corrections were applied in the microkinetic models.

The main vacancy model was a point surface oxygen vacancy (noted as V_o) as in our previous work, which corresponds to 1/4 ML surface V_o coverage on a p(2×2) surface unit cell.[28] Previous[24, 26] and current experimental TPR studies were both conducted on $CeO_{1.70}$ thin film surfaces, which corresponds to a maximum of 0.30 ML surface V_o coverage that is close to 1/4 ML. The energetics of different V_o ensembles was determined on p(4×4) surface unit cells. The surface Brillouin zones of p(2×2) and p(4×4) surface unit cells were sampled on Γ-centered 2×2×1 Monkhorst-Pack[51] k-point grid and at Γ-point only, respectively.

A mean-field microkinetic model that we previously developed was capable of producing the essential features of the AcH TPR experiment on CeO_{2-x}(111) based on DFT-calculated reaction energetic parameters. Detailed construction of the pre-factors, reaction rate constants and equilibrium constant of proposed elementary reaction steps (based on harmonic transition state theory approximations) can be found in the previous paper.[28] AcH molecules were taken to be pre-adsorbed, so the adsorption process not directly modeled while all desorption steps were taken to be irreversible under UHV conditions.

3. Results

3.1 Experimental results

In this section four experimental TPR profiles will be presented. In all cases, the vertical axis indicates molecular gas phase concentration detected by mass spectrometry during TPR. Figure 1a presents the TPR profile for AcH from oxidized $CeO_2(111)$ surface, which has a low concentration of vacancies. Consistent with previous results,[24, 26] mostly only molecular desorption of un-reacted AcH is observed at slightly above 200 K. Figure 1b shows the TPR profile for AcH on a partially reduced surface (~60% Ce^{3+}). In Figure 1b, we again see results consistent with prior studies that there are now three AcH desorption waves.[24, 26] The chemical origins of these 3 peaks are described in our prior publications: The main wave is due to molecular desorption (peak position at 210 K), the 2nd wave is due to C-O dimer decomposition (peak position at 390 K), and the 3rd wave is due to enolate recombinative desorption (peak positions between 550 K and 620 K).[26, 28] Signals associated with ethylene and acetylene were observed as minor products at temperatures similar to those reported in our previous study.[24] The relative yields of the various products are included in the Supporting Information (Tables S2a-e).

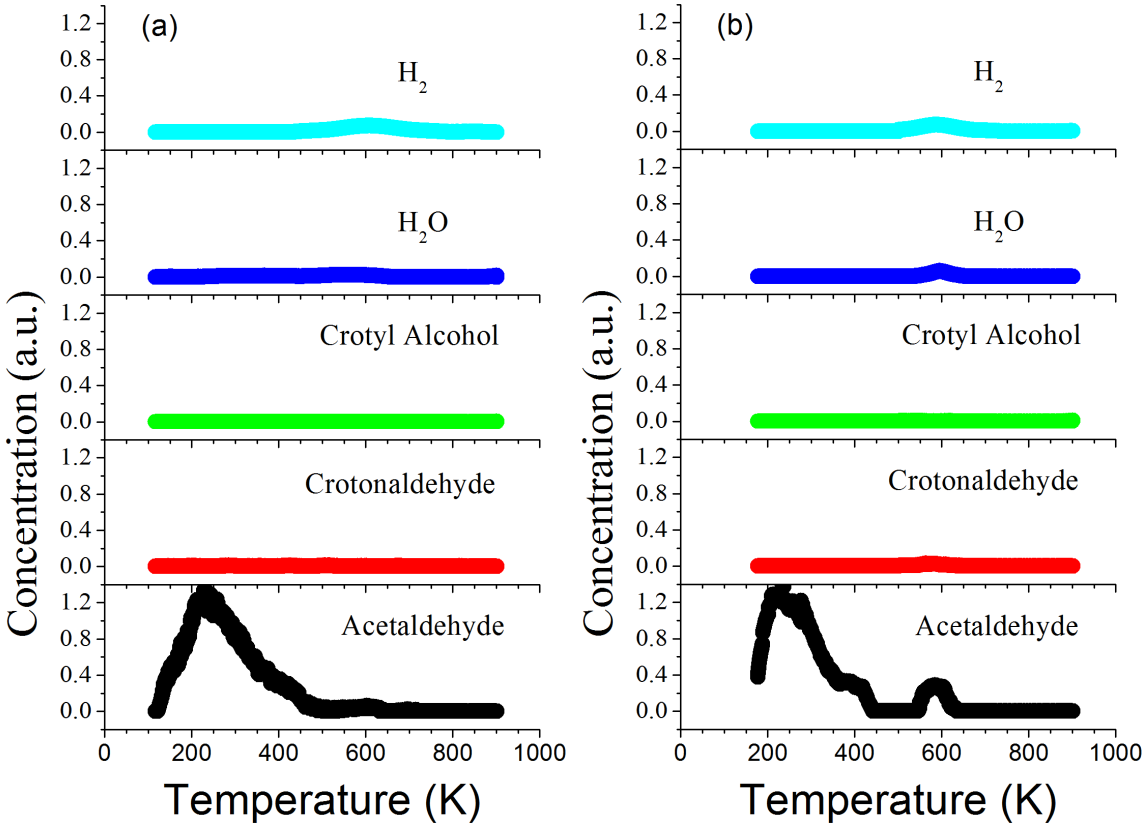

Figure 1. Gas phase concentrations of molecules detected during UHV TPR of AcH on (a) oxidized CeO_2(111) with few vacancies; (b) partially reduced CeO_{2-x}(111) with ~60% Ce^{3+}.

As our previous TPR, IR, and DFT studies concluded,[24, 26, 28] the enolate of AcH is formed on partially reduced CeO_{2-x}(111) being stabilized by an oxygen vacancy (denoted as Enl/V_o below). It has been predicted to be the dominant surface species in 400~600 K,[28] and its calculated vibrational signatures closely match RAIRS evidence in the same temperature range.[26] Enolates are well known to be the key intermediates in aldol condensation reactions, so we have devised additional experiments to attempt to realize the formation of CrA in UHV experiments.

A custom double-ramp procedure was also used. The idea behind it was to stop the experiment with the enolate on the surface and then cool down to add more AcH to allow them to react. The procedure involved a program of cooling-dosing-ramping, breaking and stopping

the ramp, then cooling-dosing-ramping again. The steps performed are as follows: 1) The surface was cooled below the monolayer adsorption temperature of AcH (160-175K) and dosed with AcH; 2) the surface temperature was ramped at 2 K/s (first ramp); 3) at a set break temperature, T_B, the heating ramp was stopped (there was no intentional dwell time at T_B, and the direction of change of the temperature reversed toward cooling on the order of seconds once the heating was stopped); 4) the surface was once again cooled below the monolayer adsorption temperature for AcH and dosed with AcH; and finally 5) the surface temperature was ramped at 2 K/s up to 900 K (second ramp).

Figure 2 shows the TPR results from the second ramp with the T_B = 410 K (Figure 2a) versus T_B = 530 K (Figure 2b). T_B = 530 K produced a clearly distinguishable CrA peak (on the order of 5% of the carbon balance), while T_B = 410 K and 460 K did not. The results of the T_B = 460 K experiments were similar to those of T_B = 410 K experiments and are shown in Supporting Information (Figure S1). In all experiments, there was little to no crotyl alcohol detected, which was consistent with the fact that crotyl alcohol was a very minor product on ceria octahedra under flow reaction conditions.[27] Enhanced H_2O production (Figure 2b) is consistent with aldol condensation, which releases two H atoms for each CrA molecule formed from AcH, although the oxygen in the water may or may not originate directly from the organic intermediates.

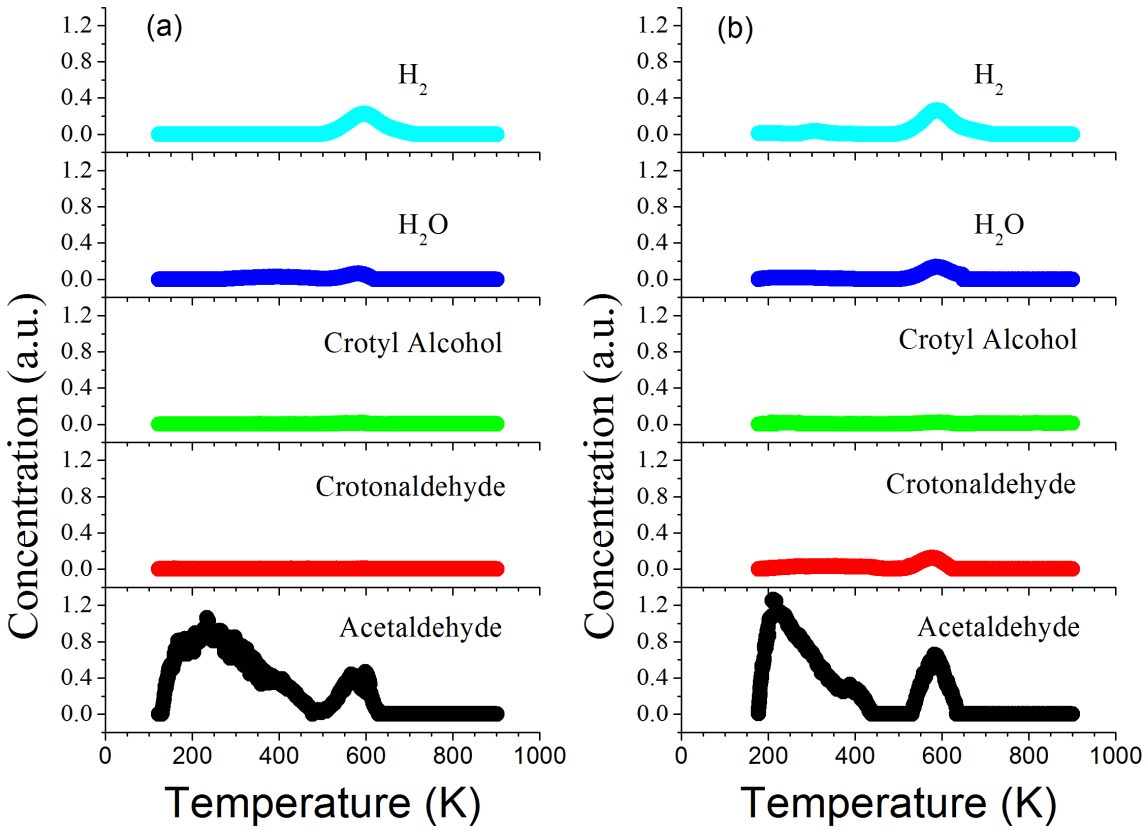

Figure 2. TPR of AcH on CeO_{2-x}(111) with ~60% Ce^{3+} for the second temperature ramp during the double-ramp procedure described in the text where the first temperature ramp was stopped at either (a) 410 K or (b) 530 K.

We conducted separate double-ramp experiments multiple times with the T_B of the first ramp at 410 K, 460 K, and 530 K, respectively. The precision for T_B was typically better than $\leq \pm 10$ K in these experiments. When T_B = 530 K was used (which implies setting T_B shortly before the peak temperature of the 3rd AcH desorption wave), significant desorption of CrA was observed. This experimental observation was reproducible and distinct to T_B = 530 K. In contrast, any CrA produced with T_B = 410 K or 460 K was either below or very near the detection limits of the experiment. The quantity of vacancies at the end of an experiment was found to be similar to at the beginning of experiment based on XPS. Furthermore, the amounts of crotonaldehyde and acetaldehyde desorption were not significantly affected when two or three of the experiments

were performed in succession, whether or not surface cleaning or regeneration was performed. Performing several experiments without cleaning is equivalent to performing several turnovers. Long-term deactivation studies were not performed.

3.2 DFT calculations for proposed mechanisms

Building on the previously elucidated mechanism for the TPR of AcH on partially reduced CeO_{2-x}(111) (Table 1),[28] we propose to extend this mechanism to include additional pathways to give three different CrA formation mechanisms that we denote as Mechanisms A, B, and C: A) coupling between Enl/V_o and AcH/V_o ; B) coupling between two Enl/V_o; C) coupling between a surface adsorbed AcH and Enl/V_o. They are all based on the hypothesis that Enl/V_o is the key reactive intermediate and must exist on the surface in order for C-C coupling to occur, while they differ in the reactant that couples to Enl/V_o. Each mechanism is restricted to a different C-C coupling pathway. By doing so, we aim to identify the main pathway of the aldol addition reaction as observed in our double-ramp experiments. The schematics in Figure 3 illustrate the three proposed TPR mechanisms.

Table 1. Previously Elucidated Mechanism and Kinetic Parameters for AcH TPD on Partially Reduced CeO_{2-x}(111),[28] Including DFT-Calculated Activation Energy (E_a, in eV), Reaction Energy (ΔE_{rxn}, in eV), and Representative Pre-Factor (ν, in s^{-1}, at 298.15 K)[#] for Each Proposed Elementary Step.

No.	Step	E_a	ΔE_{rxn}	ν
1	AcH* → AcH↑ + *	0.43	+0.43	10^{13}
2	AcH/V_o → AcH↑ + V_o	1.11	+1.11	10^{13}
3	AcH* + AcH/V_o ↔ D/VV_o	0.11	-1.57	4.11×10^{11}
4	D/VV_o + * → Enl/V_o + H* + AcH↑	1.30	+0.73	2.12×10^{13}
5	AcH/V_o + * ↔ Enl/V_o + H*	0.32	-0.91	3.72×10^{11}
6	Enl/V_o + * ↔ CHCHO/V_o + H*	1.19	+1.19	1.30×10^{12}
7	CHCHO/V_o + H* → C_2H_2↑ + H* + *	0.99	+0.43	2.45×10^{13}
8	AcH/V_o + H* ↔ Etx/V_o + *	0.67	-0.73	1.77×10^{11}
9	Etx/V_o + * ↔ CH_2CH_2O/V_o + H*	1.31	+1.30	1.55×10^{11}
10	CH_2CH_2O/V_o + H* → C_2H_4↑ + H* + *	0.17	-0.64	1.40×10^{13}
11	2H* +V_o → H_2↑ + V_o + 2*	1.75	+1.47	10^{13}

E_a and ΔE_{rxn} reported here are based on DFT total energies without ZPE correction. ΔE_{rxn} for steps involving multiple reactants or products are calculated with the multiple species at infinite separation. D denotes C-O coupled dimer of AcH. VV_o denotes a pair of adjacent surface oxygen vacancies, i.e. a vacancy dimer.

[#] Calculated in the harmonic approximation, except for desorption steps where a value of 10^{13} is used.

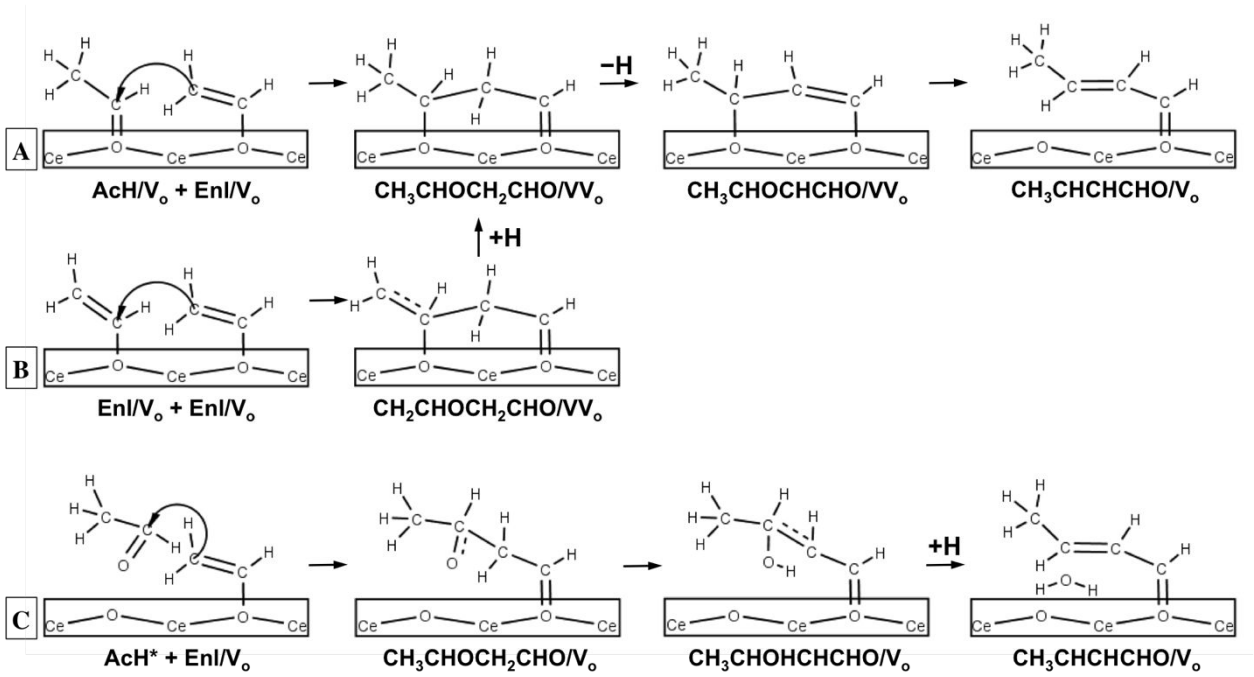

Figure 3. Schematics for extended TPR Mechanisms A, B and C. Balance of H atoms is not shown for clarity.

The extended additional steps are listed in Table 2 with their DFT-calculated energetic parameters. Below, each mechanism is presented with a reaction energy profile and the structures of the key reaction intermediates and transition states. The microkinetic modeling results for each mechanism, including simulated desorption spectra and coverage evolution of surface species are presented in the next subsection.

Table 2. Extended Steps in Mechanisms A, B, and C for AcH TPR on CeO_{2-x}(111) with DFT-Calculated Activation Energy (E_a, in eV), Reaction Energy (ΔE_{rxn}, in eV), and Representative Pre-Factor (ν, in s^{-1}, at 298.15 K)[#] for Each Proposed Elementary Step.

Mec	No.	Step	E_a	ΔE_{rxn}	ν
A	12	$Enl/V_o + AcH/V_o \leftrightarrow CH_3CHOCH_2CHO/VV_o$	0.25	-0.53	1.47×10^{11}
	13	$CH_3CHOCH_2CHO/VV_o + * \leftrightarrow CH_3CHOCHCHO/VV_o + H*$	0.65	-0.75	3.58×10^{12}
	14	$CH_3CHOCHCHO/VV_o \leftrightarrow CrA/V_o + *$	0.88	+0.38	2.69×10^{13}
B	12	$Enl/V_o + Enl/V_o \leftrightarrow CH_2CHOCH_2CHO/VV_o$	1.87	+1.80	2.92×10^{11}
	13	$CH_2CHOCH_2CHO/VV_o + H* \leftrightarrow CH_3CHOCH_2CHO/VV_o + *$	0.00	-1.41	6.21×10^{12}
	14-15	same as A13-A14			
C	12	$Enl/V_o + AcH* \leftrightarrow CH_3CHOCH_2CHO/V_o$	0.22	+0.13	8.07×10^{9}
	13	$CH_3CHOCH_2CHO/V_o \leftrightarrow CH_3CHOHCHCHO/V_o$	1.03	-0.56	7.08×10^{11}
	14	$CH_3CHOHCHCHO/V_o \leftrightarrow CrA/V_o + OH*$	1.20	+1.10	1.33×10^{14}
	15	$CrA/V_o + OH* + H* \leftrightarrow CrA/V_o + H_2O*$	0.10	-0.07	1.05×10^{12}
	16	$H_2O* \rightarrow H_2O\uparrow$	0.52	+0.52	10^{13}
Des.		$CrA/V_o \rightarrow CrA\uparrow + V_o$	2.12	+2.12	10^{13}

E_a and ΔE_{rxn} reported are based on DFT total energies without ZPE corrections. CrA desorption is common to all three mechanisms as the final step.

[#] Calculated in the harmonic approximation, except for desorption steps where a value of 10^{13} is used.

In Mechanism A, C-C coupling occurs between AcH/V_o and Enl/V_o (Figures 4a, e) to produce CH_3CHOCH_2CHO (Figure 4b), which occupies a pair of adjacent surface oxygen vacancies (VV_o) and a surface H, with a small E_a of 0.25 eV. The methylene group ($-CH_2-$) undergoes H abstraction (Figure 4f) with a nearby lattice oxygen as the H acceptor, with E_a = 0.65 eV. The product, $CH_3CHOCHCHO/VV_o$ (Figure 4c), undergoes C-O scission (E_a = 0.88 eV) that cleaves off the internal oxygen, which yields a vacancy-stabilized CrA (CrA/V_o, Figure 4d) and

annihilates one oxygen vacancy. The final step is desorption of CrA from V_o, which is common to all three expanded TPR mechanisms. The desorption barrier is taken to be the reverse of the adsorption energy, which is calculated to be -1.35 eV (GGA-PW91) and -2.12 eV (optB86-vdW). The negative of the latter is used in the microkinetic modeling as the desorption barrier for CrA because it yields far better agreement with the experimental peak temperature for CrA than the GGA value. We note that optB86b-vdW is known to overbind molecules somewhat on metals[52] but there is so far no database of reliable experimentally measured heats of chemisorption on oxides to gauge how accurate this functional is for adsorption on ceria. The strong interaction of the carbonyl intermediates with V_o on CeO_2(111) is a reason why alcohol species such as crotyl alcohol and ethanol do not appear as major products in the current and prior experiments,[27] since the hydrogenation of the vacancy-stabilized C=O group is likely a difficult step.

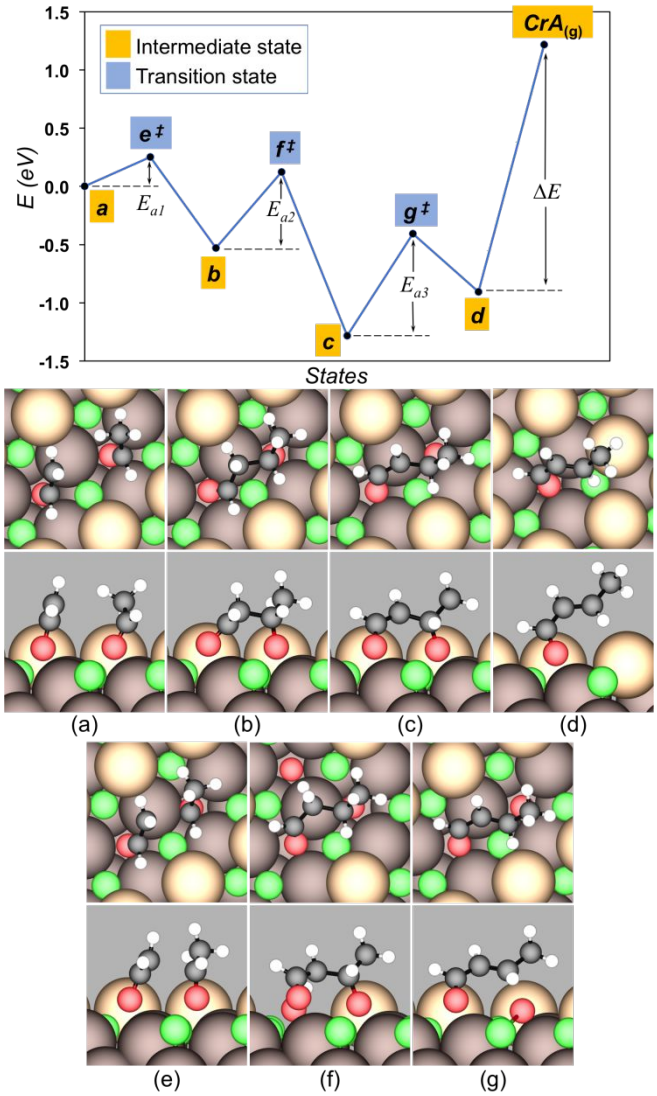

Figure 4. Extended steps of TPR Mechanism A. (Upper) DFT-calculated reaction total energy profile. The labeled states are: (a) Enl/V_o+AcH/V_o; (b) CH_3CHOCH_2CHO/VV_o; (c) $CH_3CHOCHCHO/VV_o$; (d) CrA/V_o; (e) TS for C-C coupling; (f) TS for H abstraction; (g) TS for C-O scission. "‡" denotes a TS. The forward E_a's are E_{a1} = 0.25 eV, E_{a2} = 0.65 eV, E_{a3} = 0.88 eV, and ΔE = 2.12 eV. (Lower) Snapshots of reaction intermediates and transition states, with top view on top and side view on bottom. Labels correspond to those in the upper panel. Green, light brown, dark brown, red, black, and white spheres represent lattice Ce, surface lattice O, subsurface lattice O, O in molecules, C, and H atoms, respectively. Molecular images in this figure and those below are created using VESTA.[53] Surface lattice O atoms bonded to C or H

atoms in the molecules are considered part of the molecules. Periodic images of the adsorbates have been removed for clarity.

In Mechanism B, a pair of adjacent vacancy-stabilized Enl/V_o (Figures 5a, f) undergo self-coupling by overcoming a substantial E_a of 1.87 eV, forming CH_2CHOCH_2CHO/VV_o (Figure 5b). Afterwards a surface H atom is transferred with practically zero barrier from a lattice O site to the terminal methylene group of CH_2CHOCH_2CHO/VV_o, forming CH_3CHOCH_2CHO/VV_o (Figure 5c). The subsequent steps are identical to Mechanism A following the formation of CH_3CHOCH_2CHO/VV_o, although the prior steps in Mechanism A, i.e. C-C coupling between Enl/V_o and AcH/V_o, are not included here.

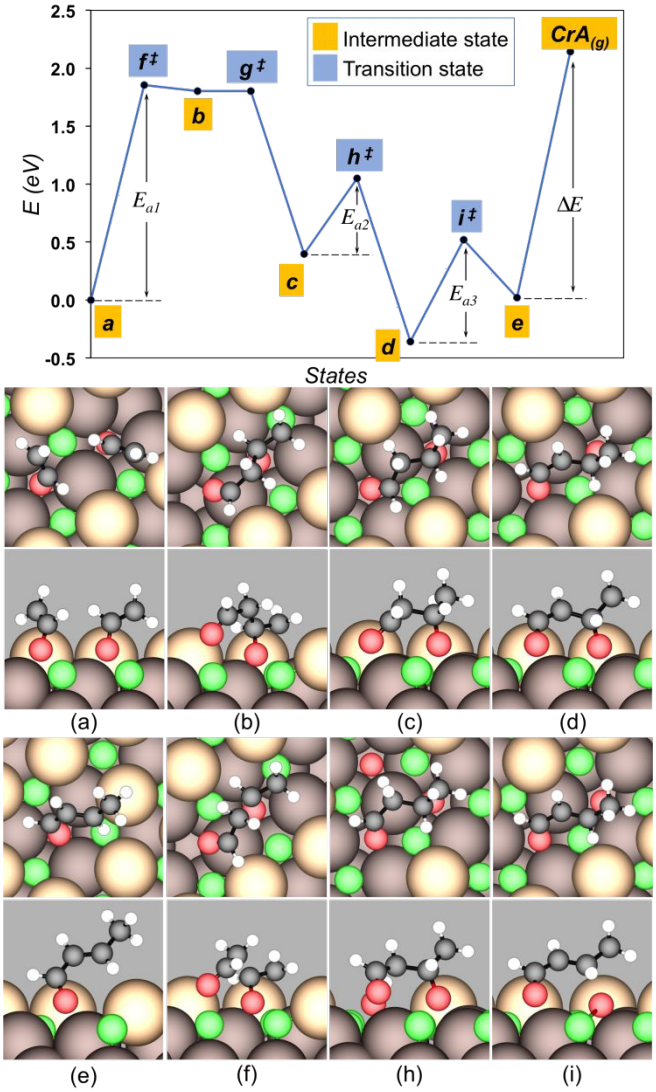

Figure 5. Extended steps of TPR Mechanism B. (Upper) DFT-calculated reaction total energy profile. The labeled states are: (a) Enl/V_o+Enl/V_o; (b) CH_2CHOCH_2CHO/VV_o; (c) CH_3CHOCH_2CHO/VV_o; (d) $CH_3CHOCHCHO/VV_o$; (e) CrA/V_o; (f) TS for C-C coupling; (g) TS for H addition (not shown in snapshots due to zero barrier); (h) TS for H abstraction; (i) TS for C-O scission. "‡" denotes a TS. The forward E_a's are E_{a1} = 1.87 eV, E_{a2} = 0.65 eV, E_{a3} = 0.88 eV, and ΔE = 2.12 eV. (Lower) Snapshots of reaction intermediates and transition states, with top view on top and side view on bottom. Labels correspond to those in the upper panel. Green, light brown, dark brown, red, black, and white spheres represent lattice Ce, surface lattice O, subsurface lattice O, O in molecules, C, and H atoms, respectively. Surface lattice O atoms

bonded to C or H atoms in the molecules are considered part of the molecules. Periodic images of the adsorbates have been removed for clarity.

In Mechanism C, the C-C coupling step occurs between surface-adsorbed AcH* and vacancy-stabilized Enl/V_o. Thus this mechanism requires only one surface oxygen vacancy rather than a vacancy dimer as in Mechanisms A and B. As shown in Table 2, the C-C coupling step only needs to overcome an activation energy of 0.22 eV, with a corresponding ΔE_{rxn} of +0.13 eV. The product of the C-C coupling step, CH_3CHOCH_2CHO/V_o (Figure 6b), is less stable than the C-O coupled dimer and prone to decomposition. The most facile pathway to CrA formation involves intra-molecular H transfer (from the methylene group to the internal carbonyl O) with E_a = 1.03 eV to yield a vinyl alcohol species, $CH_3CHOHCHCHO/V_o$ (Figure 6c), and the OH group then dissociating with E_a = 1.20 eV. OH can scavenge a nearby surface H to form water, which readily desorbs from the surface (ΔE_{ads} = -0.52 eV).

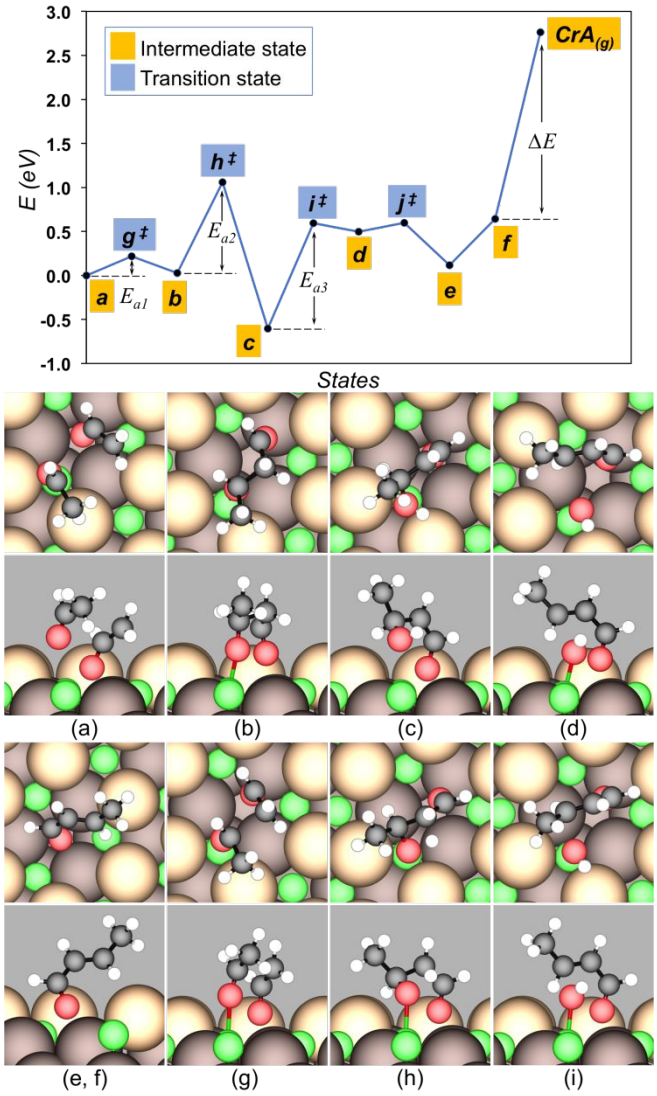

Figure 6. Extended steps of TPR Mechanism C. (Upper) DFT-calculated reaction total energy profile. The labeled states are: (a) Enl/V_o+AcH*; (b) CH_3CHOCH_2CHO/V_o; (c) $CH_3CHOHCHCHO/V_o$; (d) CrA/V_o+OH*; (e) CrA/V_o, H_2O*; (f) CrA/V_o, H_2O^{gas}; (g) TS for C-C coupling; (h) TS for intra-molecular H transfer; (i) TS for OH detaching; (j) TS for water formation. (e) and (f) are shown without any coadsorbate. "‡" denotes a TS. The forward E_a's are E_{a1} = 0.22 eV, E_{a2} = 1.03 eV, E_{a3} = 1.20 eV, and ΔE = 2.12 eV. (Lower) Snapshots of reaction intermediates and transition states, with top view on top and side view on bottom. Labels correspond to those in the upper panel. Green, light brown, dark brown, red, black, and white spheres represent lattice Ce, surface lattice O, subsurface lattice O, O in molecules, C, and

H atoms, respectively. Surface lattice O atoms bonded to C or H atoms in the molecules are considered part of the molecules. Periodic images of the adsorbates have been removed for clarity.

3.3 Microkinetic modeling

Our microkinetic modeling effort based on the three TPR mechanisms is aimed at reproducing and explaining the results observed in the second ramp of the double-ramp experiments. The coverages at the start of the second ramp are specified in the caption of Figure 7. They are the final results of the microkinetic model of our original TPR mechanism by terminating the temperature ramp at 603 K, i.e., at the peak of the 3rd AcH desorption wave in the original microkinetic model, so that a certain portion of the occupied V_o becomes unoccupied and available to be occupied by AcH in the second dosing. Therefore, a mixture of the enolate and AcH occupy all of the V_o sites at the beginning of the simulated second ramp. The total coverage of V_o (0.226 ML) is less than the initial coverage of V_o used in the original microkinetic model (0.3 ML) because a portion of V_o has been annihilated in the reductive desorption of the C_2 products. Residual atomic H and newly dosed molecular AcH take up most of the oxidized sites. The starting temperature and ramping rate are identical to those used in the original model.[28]

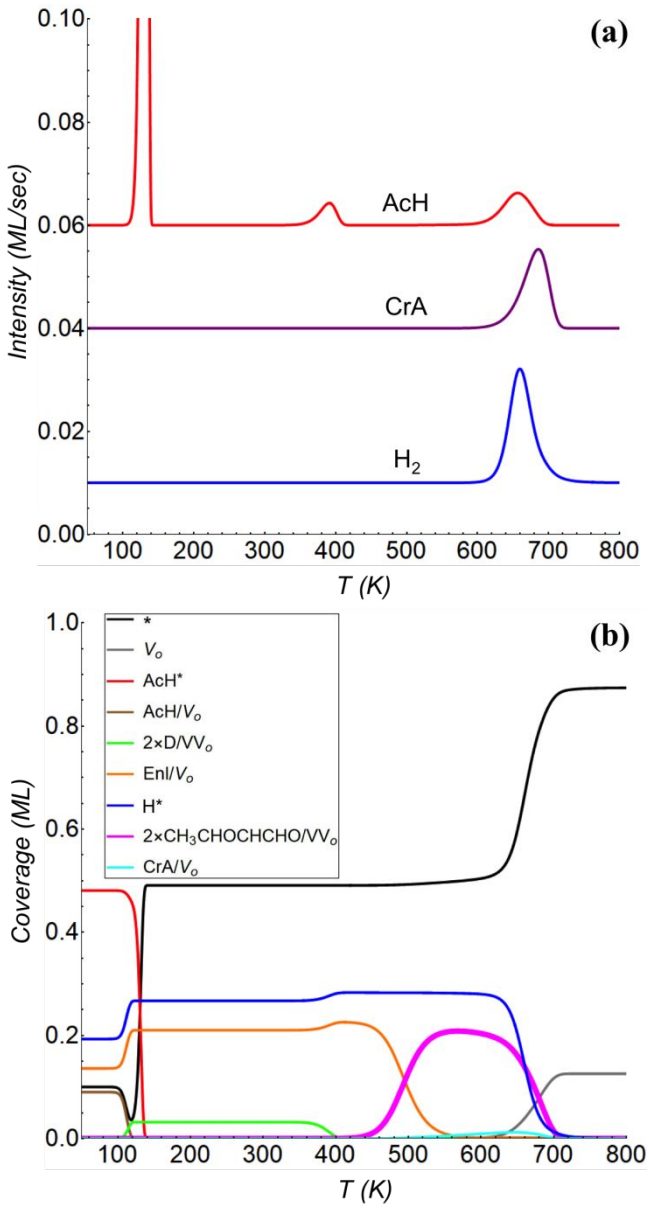

Figure 7. (a) Simulated TPR spectra and (b) corresponding coverages of surface intermediates as a function of temperature for AcH on partially reduced CeO_{2-x}(111) based on microkinetic modeling of TPR Mechanism A. Initial coverages (in ML): EnI/V_o = 0.136; AcH/V_o = 0.090; H* = 0.193; AcH* = 0.481; all other intermediates = 0; free V_o = 0; free site (*) set to 0.1. T_0 = 50 K; ramp rate = 2 K/s. Surface intermediates with essentially 0 ML coverages are not shown in (b).

The simulated TPR spectra based on Mechanism A are shown in Figure 7a. Three AcH desorption peaks are predicted, with peak temperatures (T_p) of 132, 391, and 656 K. As mentioned before, the origin for the 1st AcH wave is the molecular desorption of AcH. The 2nd AcH wave is due to the decomposition of a C-O coupled dimer (D/VV_o), which releases an AcH molecule to the gas phase under UHV conditions. The 3rd AcH wave is due to the recombinative desorption of Enl/V_o and H. Compared to the our original TPR mechanism,[28] the 3rd AcH peak temperature here is higher by ~50 K, which also applies to molecular hydrogen with T_p = 660 K (previously 620 K). The desorption wave for CrA is predicted to span from ca. 590 K to 720 K, with T_p = 686 K.

Microkinetic modeling also predicts how the coverages of surface species evolve as a function of temperature. For Mechanism A (Figure 7b), it can be seen that all the additional AcH added for the second temperature ramp has disappeared by ca. 130 K, due to either molecular desorption or enolization (with a concomitant increase in the coverage of Enl/V_o). Between ca. 130 K and 500 K the enolate is the dominant C-containing surface species. Above ca. 450 K, the C-C coupling pathway is actuated to generate $CH_3CHOCHCHO/VV_o$, which becomes a dominant surface species between ca. 500 K and 700 K. This happens because the enolate begins to recombine with H to form AcH/V_o, which then rapidly undergoes C-C coupling with other Enl/V_o but does not build up any appreciable coverage. A small coverage of CrA/V_o also builds up between ca. 550 K and 700 K. All other organic intermediates are predicted to have negligible coverages. At the end of the temperature ramp ca. 0.1 ML of oxygen vacancy (out of the initial 0.226 ML) is annihilated on account mainly of CrA formation.

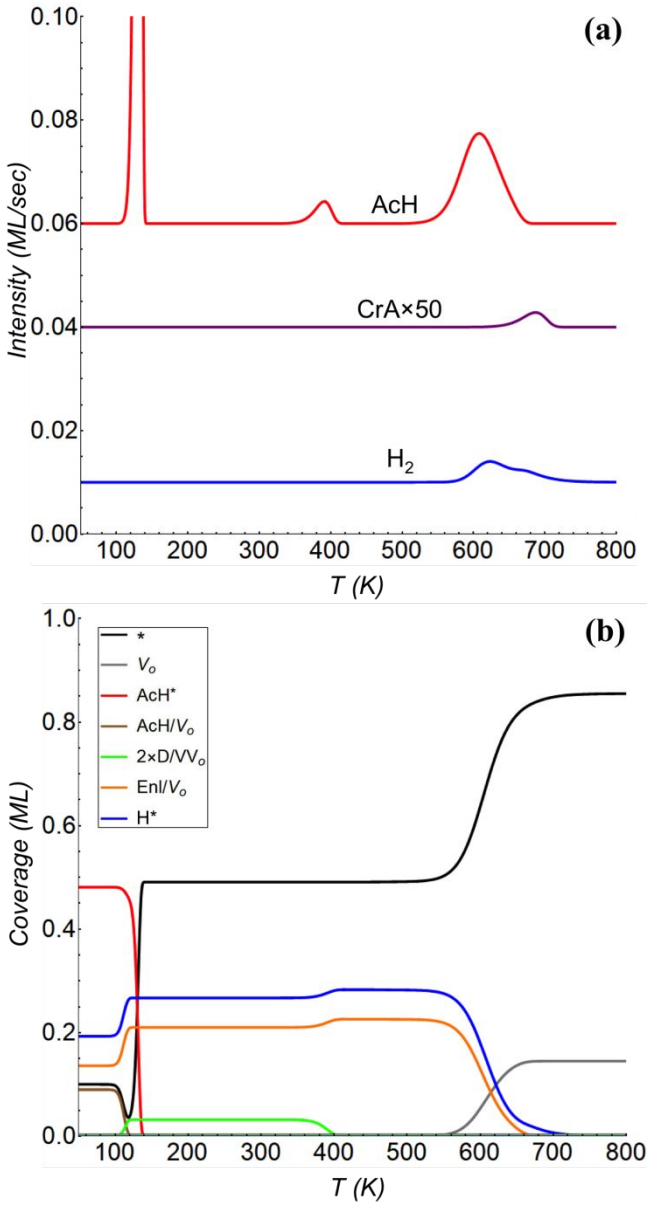

Figure 8. (a) Simulated TPR spectra and (b) corresponding coverages of surface intermediates as a function of temperature for AcH on partially reduced CeO_{2-x}(111) based on microkinetic modeling of TPR Mechanism B. Initial conditions and ramp rate are identical to those in Figure 7. Surface intermediates with essentially 0 ML coverages are not shown in (b).

The results of microkinetic modeling for Mechanism B are markedly different from those of Mechanism A. As shown in Figure 8a, the 3rd AcH wave has a T_p = 608 K and a greater peak

area than the 2nd AcH peak. CrA desorption occurs with a nearly identical T_p to Mechanism A, but it is significantly diminished in intensity. These results are similar to the microkinetic modeling results of our original AcH TPR mechanism[28] because the C-C coupling pathway is essentially not operative in Mechanism B due to the high activation energy for the enolate self-coupling step. This is confirmed by the evolution of the coverages of surface species, which indicates that none of the C_4 intermediates ~~have~~ any appreciable coverage over the entire temperature range in Mechanism B (and therefore not shown in Figure 8b). Combining Mechanisms A and B yields results essentially identical to Mechanism A alone.

No CrA desorption is predicted in the simulated TPR based on Mechanism C (Figure 9a). The reason why Mechanism C fails to produce CrA is that the C-C coupling product, CH_3CHOCH_2CHO/V_o, readily breaks down and back into Enl/V_o and AcH. The other desorption features are mostly identical to those based on Mechanism B.

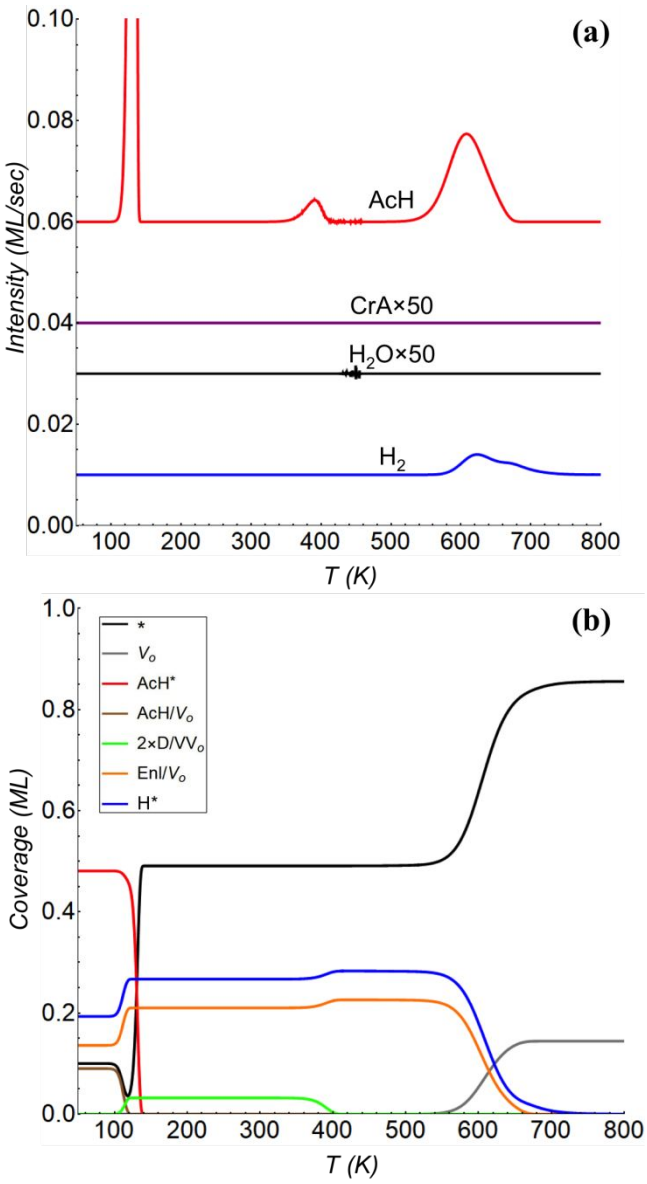

Figure 9. (a) Simulated TPR spectra and (b) corresponding coverages of surface intermediates as a function of temperature for AcH on partially reduced CeO_{2-x}(111) based on microkinetic modeling of TPR Mechanism C. Initial conditions and ramp rate are identical to those in Figure 7. Surface intermediates with essentially 0 ML coverages are not shown in (b).

Overall, therefore, Mechanism A yields the best agreement with the double-ramp experiments on CeO_{2-x}(111) with T_B = 530 K. The essential features of this mechanism are: 1) The C-C

coupling step occurs in a pair of surface oxygen vacancies. The site requirement is further discussed below. 2) CrA desorption, and not C-C coupling, is rate-limiting. We have estimated that, if CrA desorption were not rate-limiting, the T_p of CrA desorption would be 493 K.

Note that ethylene and acetylene channels remain part of the expanded mechanisms, although their production, together with high-temperature AcH formation, is reduced compared to the original TPD model[28] (see Figure S2 for the C_2H_4 and C_2H_2 traces in the simulated TPR for Mechanism A). This is consistent with the outcome of the double-ramp experiments, which found ethylene and acetylene to be minor products (especially the latter; see Tables S2a-e). We attribute the difference to the existence of the CrA channel, which removes a portion of the enolates from the uni-molecular pathways that produce AcH, ethylene, and acetylene. Of these, only the desorption of the organics as C_2H_2 permits H to desorb as H_2, so the diminishment of acetylene formation means less contribution to H_2 evolution from the uni-molecular pathways. Meanwhile, the formation of each CrA molecule from two AcH molecules discharges a net total of two H atoms, so an H_2 peak similar in size to the CrA peak should be expected and is indeed predicted by our microkinetic model for Mechanism A. No H_2O channel is provided by Mechanism A whereas on the actual ceria surface some atomic H is almost certainly diverted from desorption as H_2 to reduction of the surface (e.g. at loosely bound lattice O sites).

4. Discussion

4.1 Aldol condensation mechanisms

As mentioned earlier, aldol condensation is typically conceived of as proceeding through either an acid mechanism or a base mechanism. Below we will describe the type of mechanism with the nomenclature of Nucleophile ^ Electrophile (with the two species listed in that order). Acid-

catalyzed aldol condensation proceeds through a nucleophilic enol intermediate, and we denote the mechanism as Enol ^ Keto cation (A_A, Figure 10). An acid catalyzes this route by withdrawing electron density from the carbonyl carbon on the molecule being attacked, thus making the carbonyl carbon of the second molecule an electrophilic center. In contrast, base-catalyzed aldol condensation proceeds through the Enolate ^ Keto mechanism (A_B, Figure 10) by proton abstraction from a keto by a base (where keto refers to either a ketone or an aldehyde), resulting in an enolate anion (the enolate anion has hybridization so there is no separate keto anion since it is simply a resonance structure rather than a tautomer). In all cases, an enolate or enol moiety is the nucleophile, and a keto or keto cation moiety is the electrophile. In aqueous phase, the keto cation or the enolate anion is primarily stabilized by solvation effects and also by weak coordination by the counter-ion of the acid or base, respectively.

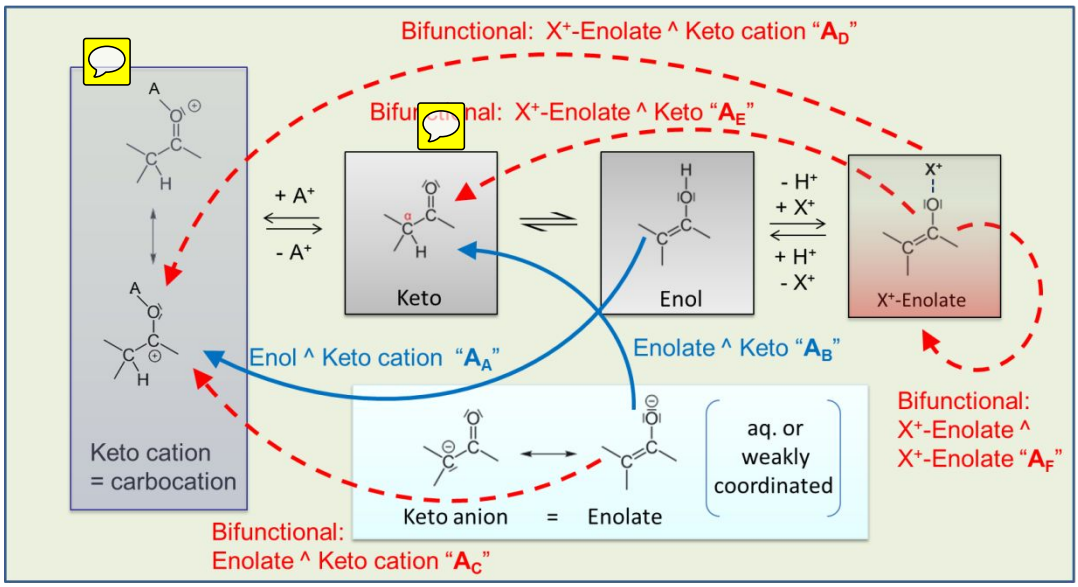

Figure 10. Different possible mechanisms for aldol condensation mechanisms, labeled with the nomenclature of Nucleophile ^ Electrophile. The conventional aqueous phase Enol ^ Keto cation and Enolate ^ Keto mechanisms are labeled as "A_A" and "A_B" respectively. The other mechanisms may be made accessible through bifunctional/multifunctional heterogeneous catalysis.

Reducible oxide surfaces such as CeO_2(111) open up the possibility of a type of enol-keto chemistry subtly different from its aqueous phase counterpart. Here a metal cation site (which is acidic) ~~takes the~~ place ~~of~~ water as solvent to directly stabilize the carbonyl ~~carbon~~ of a keto species, and an oxygen anion site (which is basic) performs hydrogen abstraction, resulting in the formation of an X^+-Enolate intermediate (Figure 10). Thus, as over other oxides, it is a bifunctional mechanism requiring both acid and base sites to participate in the reaction. This study continues in the tradition of investigating aldol condensation on heterogeneous catalysts at the molecular level with basic oxides[5-7, 9-17] and rationally designed acid-and-base bifunctional catalysts,[12, 14-17] although unlike basic or promoted oxides, ceria surfaces natively feature evenly distributed acid and base sites in close proximity.

Prior work has shown CrA formation by aldol condensation of AcH to be possible on CeO_2(100) single crystal surfaces under well-controlled UHV conditions,[25] on polycrystalline ceria under low pressure, as well as on other chemically related oxides. For instance, a small CrA peak (<5% of the carbon balance) was observed during TPR of AcH from a fully oxidized CeO_2(100) surface, but the presence of oxygen vacancies apparently suppressed CrA formation so that it was not observed on a partially reduced CeO_2(100) surface.[25] Consistent with the current view, Mullins et al. suggested that a dioxyethylene species is the direct precursor from which H is abstracted by surface oxygen sites to form a short-lived metastable enolate, which then acts as the nucleophile during coupling.[25] It stands to reason that removing surface oxygen atoms results in a decrease in the ability of the surface to abstract hydrogen from the CH_3 group, and thus a decrease in enolate formation and C-C coupling.

The chemistry of AcH on CeO_2(111) and CeO_{2-x}(111) in TPR stands in contrast to that on the CeO_2(100) surfaces: On fully oxidized CeO_2(111) little reaction of AcH was observed, whereas the enolization of AcH readily occurred on CeO_{2-x}(111). The enolate of AcH proved to be very stable under UHV conditions in a typical TPR procedure and was readily detected by infrared spectroscopy and x-ray photoelectron spectroscopy at temperatures between 400 K and 550 K.[26] We surmise that part of the difference is due to the fact that Ce cation sites are less accessible on CeO_2(111) than on CeO_2(100) unless oxygen vacancies are created, with each point vacancy partially exposing three Ce cations to facilitate the formation of X^+-Enolate intermediates.

The double-ramp experiments in the present study reveal that AcH can undergo C-C coupling on CeO_2(111) as well. The DFT calculations and the microkinetic modeling based thereon show that the experimental TPR data are consistent with an X^+-Enolate ^ Keto cation mechanism (A_D in Figure 10) that requires an oxygen vacancy for the formation of X^+-Enolate to act as a nucleophile, and an adjacent oxygen vacancy to stabilize another carbonyl molecule to act as an electrophile. The fact that CrA is formed at a far greater rate in Mechanism A (via Enl/V_o+AcH/V_o) than in Mechanism B (via Enl/V_o+Enl/V_o) during simulations is consistent with the fact that the enolate functions primarily as a nucleophile, not as an electrophile, and self-coupling of the enolate is therefore not as effective as coupling between Enl/V_o and AcH/V_o. In comparison, partially exposed arrays of Ce cation sites already exist on CeO_2(100), so AcH can enolize without oxygen vacancies and couple with other adjacent, X^+-stabilized AcH molecules on CeO_2(100) in a typical, single-ramp TPR procedure.

4.2 Energetics for vacancy clustering

We attribute the face that no CrA was detected in the single-ramp experiments[26] to the fact that, as alluded to before, the positioning of oxygen vacancies is crucial to the bimolecular coupling step. A key requirement implicit in Mechanisms A and B (but not C) is that Enl/V_o and AcH/V_o or another Enl/V_o must be adjacent to each other in order for aldol addition and CrA formation to occur effectively. If Enl/V_o is instead surrounded by oxygen sites, C-C coupling can still occur (e.g. via Mechanism C), but it would not lead to CrA formation under UHV conditions due to the decomposition of intermediates.

The nature of oxygen vacancies on CeO_2(111) has long been debated in the literature. Early work based on scanning tunneling microscopy (STM) and atomic force microscopy (AFM) for high-temperature annealed CeO_2(111) single crystal surfaces reported a predominance of surface and subsurface oxygen vacancy clusters, while point surface vacancies appeared to be a minority species.[54-55] More recently it was demonstrated theoretically that previous STM studies were not capable of distinguishing oxygen vacancies from fluorine impurities, which are typically present at appreciable concentrations in naturally occurring CeO_2, and that the vacancy clusters seen in STM may be clusters of fluorine atoms.[56] DFT studies based on GGA,[57-58] GGA+U (U=4.5~5 eV),[59-61] and HSE06 hybrid functional[59] all reported that an isolated oxygen point vacancy to be a few tenths of an eV more stable in subsurface than in surface. GGA+U also predicted point vacancies to be more stable than vacancy clusters, whether on surface or in subsurface. Forming a surface vacancy dimer from two surface point vacancies is calculated to be endothermic by +0.16 eV by Murgida et al. and +0.34 eV by Conesa.[60, 62]

Based on the latest findings, we surmise that the as-synthesized CeO_{2-x}(111) films used in our experiments initially (Figure 1b) contained primarily isolated vacancies and few vacancy clusters

since they are disfavored by thermodynamics. When AcH was dosed onto such a surface, all point vacancies should be occupied by AcH and later the enolate molecules, which immobilized the vacancies. Mechanisms A and B would be largely inoperative on such a CeO_{2-x}(111) surface. For clusters of oxygen vacancies to appear, the following conditions must be met:

1. Some AcH molecules desorb to vacate some vacancies;
2. Vacancies are able to diffuse at an appreciable rate;
3. The energetics is altered to favor the aggregation of vacancies.

What the double-ramp experiments with T_B = 530 K accomplish (Figure 2b), thus, is to free some vacancies while retaining some enolate molecules in vacancies as the third AcH desorption wave is under way by 530 K. When vacancies become unoccupied appear at 530 K, their mobility is expected to be high because the diffusion barrier for oxygen vacancies via a surface-subsurface exchange mechanism has been calculated theoretically to be modest (E_a = 0.5 or 0.6 eV with GGA+U with U=3 [63] or 5 [64] respectively). Further, our calculations show that the occupation of a surface V_o by an enolate can make the formation of a surface vacancy dimer *exothermic*, in contrast to the dimerization of two unoccupied surface point vacancies.[60, 62] As summarized in Table 3, when an enolate occupies a surface V_o, the energetics of a second, unoccupied V_o varies depending on its location, with the site in the surface that is nearest neighbor to Enl/V_o being the most favorable. In other words, neighbor-neighbor interaction between Enl/V_o and an unoccupied V_o (similar to adsorbate-adsorbate effects if V_o were considered an adsorbate) alters which state is thermodynamically favored relative to the energetics in the absence of the enolate. Conversely, if most of the enolates desorb, the thermodynamics would cause most such vacancy dimers to re-disperse. We note this stabilization does not extend to the formation of a vacancy trimer: The energy of adding a third,

unoccupied surface V_o to an existing Enl/VV_o (enolate-occupied vacancy dimer) is calculated to be +0.55 and +0.37 eV (U = 2 and 5 eV, respectively).

Table 3. Location, Energy (E_v, in eV), and Boltzmann Probability (P, in %, calculated at 603 K) for an Unoccupied Oxygen Vacancy in the Presence of an Enl/V_o species on CeO_2(111) at U = 2 and 5 eV

	U = 2		U = 5	
location of 2nd V_o [a]	E_v [b]	P	E_v [b]	P
N.N., surface	-0.03	60	-0.13	91
N.N., subsurface	+0.27	0	+0.27	0
Inf. Sep., surface	+0.05	9	+0.01	4
Inf. Sep., subsurface	0	31	0	5

[a] Relative to the location of the enolate occupied V_o. N.N. = nearest neighbor, Inf. Sep. = infinite separation.

[b] Based on DFT total energy without ZPE correction, relative to the Inf. Sep., subsurface state.

In short, all three conditions above can be met if the first temperature ramp is terminated at an appropriate temperature, resulting in the formation of partially occupied surface vacancy dimers that allow the enolate molecules to be stabilized side-by-side in vacancies, in a position to undergo effective adol addition in the second temperature ramp. Using a lower T_B (e.g. 410 K or 460 K) in the first ramp does not lead to CrA formation (Figure 2a) because all vacancies are still occupied by the enolates and cannot aggregate to form vacancy dimers.

4.3 Treatment of atomic H

Adsorbate-adsorbate interaction is an aspect of surface chemical kinetics that conventional microkinetic modeling is not capable of fully handling. As the theoretical results above show, there are comparable coverages of some organic intermediate and atomic H (ca. 0.2~0.3 ML) between ca. 100 K and 600~700 K (Figures 7-9, depending on the mechanism). The interaction between the organic intermediates and atomic H turns out to be moderately repulsive in all cases (Table S3). On the basis of that, and for consistency with our previous microkinetic model,[28] we have treated the organic intermediates and H to have no interaction, or "at infinite separation", in the present models. OH has a very strong stabilizing interaction with both CrA/V_o and H, so they are treated as coadsorbates in the models.

It should be noted, however, that the diffusion barrier for atomic H on $CeO_2(111)$ has been determined theoretically to be 1.8 eV (GGA+U; U=4.5),[65] which means that the mobility of H is highly limited below 600 K according to DFT, in stark contrast to H on metal surfaces. The coverage of H is therefore likely to be locally non-equilibrated on the surface due to reactions, which complicates the estimation of coverage dependence for reaction energetics, if such an approach were to be used in microkinetic modeling. The fact that the H_2 and H_2O desorption waves appear to be linked (Figure 2b) may also be due to a common underlying process, e.g. H atoms diffusing in search of H_2 formation sites or loosely bound O anions. If true, our TPR results would suggest the GGA+U diffusion barrier of 1.8 eV reported in the literature to be overestimated by ca. 0.2~0.3 eV, but we are unable to confirm it by locating a lower diffusion barrier on $CeO_2(111)$ theoretically.

To fully account for all of these effects would require a comprehensive kinetic Monte Carlo model with reaction energetic parameters implemented as explicit functions of local coverages of

atomic H, organic intermediates, and surface oxygen vacancies, and with the mobility of H and oxygen vacancies taken into account. It is outside the scope of the present study. While our simple microkinetic approach undoubtedly contains inaccuracies, the purpose of adopting it is to show that the aldol addition mechanism that we propose is fundamentally compatible with the experimental TPR, which sheds light on the microscopic level intricacies of this reaction.

5. Conclusions

In this work, we have presented a new mechanism for crotonaldehyde (CrA) formation from acetaldehyde (AcH) that is promoted by oxygen vacancy dimers on CeO_2(111). CeO_2 particles have previously been shown to produce CrA under low pressure[9] and flow reaction conditions,[27] and now CrA formation has been observed on CeO_2(111) surfaces using tailored double-ramp TPR experiments under well-controlled conditions.

Based on the experimental evidence and DFT-based microkinetic modeling, the pathway accessed is suggested to be of the X^+-Enolate ^ Keto cation type, with the C-C coupling step occurring between an X^+-Enolate formed from AcH and a second (dynamically re-formed) AcH molecule, with the two species located side-by-side in a pair of oxygen vacancies. DFT calculations further suggest that the active site (a surface oxygen vacancy dimer) forms due to altered vacancy stability, as an enolate-occupied oxygen vacancy attracts, rather than repels, a second oxygen vacancy. Such vacancy dimers are created *in situ* upon partial AcH desorption at appropriately elevated temperatures, a crucial detail that cannot be easily revealed without a combination of UHV experiments based on the special procedure that we have developed and first-principles-based theoretical and computational modeling.

Given that multiple mechanisms are possible for CrA, the present work adds knowledge to the literature by showing that an X^+-Enolate ^ Keto cation mechanism (A_D in Figure 10) is experimentally accessible on CeO_2(111), and that the dynamic nature of oxygen vacancies plays a key role. This elucidated mechanistic pathway requires an active site ensemble consisting of multiple surface elements (i.e. lattice Ce cations and oxygen anions, surface oxygen vacancies, and pre-adsorbed enolates), which may be amenable to tuning on CeO_2(111) and possibly on other reducible oxide surfaces, for the design of multifunctional catalysts for aldol condensation reactions. We are not aware of prior evidence published for an aldol condensation mechanism involving oxygen vacancies, as presented in this study. We believe that these findings have general relevance for the discovery of future generations of catalysts for upgrading organic molecules derived from biomass conversion, for example, in producing partially oxygenated coupling products under reducing conditions.

Acknowledgments

The work at Oak Ridge National Laboratory (experiments, mass spectrometry analysis) was supported by the U.S. Department of Energy, Office of Science, Basic Energy Sciences, Chemical Sciences, Geosciences, and Biosciences Division, under contract DE-AC05-00OR22725. Initial calculations by P.K. were conducted at the Center for Nanophase Materials Sciences, which is a US-DOE Office of Science User Facility. C.W. was supported by the US-DOE, Office of Science, Office of Workforce Development for Teachers and Scientists (WDTS) under the Science Undergraduate Laboratory Internships Program (SULI) program at Oak Ridge National Laboratory, administered by the Oak Ridge Institute for Science and Education. The work at Louisiana State University (computational modeling, theoretical analysis) was supported

by the U.S. National Science Foundation under Grant #CHE-1664984, and used high performance computational resources provided by LSU (https://hpc.lsu.edu), by the Center for Nanophase Materials Sciences, which is a US-DOE Office of Science User Facility, and by the National Energy Research Scientific Computing Center, which is supported by the Office of Science of US-DOE under Contract No. DE-AC02-05CH11231.

Supporting Information

The Supporting Information is available free of charge on the ACS Publications website at DOI:

1) Final mass spectrometry reference patterns used in analysis; 2) Relative yields of products observed during TPR; 3) TPR spectra for second ramp with T_B = 460 K; 4) Simulated TPR spectra showing ethylene and acetylene; 5) Interaction energies between organic intermediates and atomic H.

References

1. Wu, L.; Moteki, T.; Gokhale, A. A.; Flaherty, D. W.; Toste, F. D., Production of Fuels and Chemicals from Biomass: Condensation Reactions and Beyond. *Chem* **2016,** *1*, 32-58.

2. Resasco, D. E., What Should We Demand from the Catalysts Responsible for Upgrading Biomass Pyrolysis Oil? *J. Phys. Chem. Lett.* **2011,** *2*, 2294-2295.

3. Huber, G. W.; Chheda, J. N.; Barrett, C. J.; Dumesic, J. A., Production of Liquid Alkanes by Aqueous-Phase Processing of Biomass-Derived Carbohydrates. *Science* **2005,** *308*, 1446-1450.

4. Nielsen, A. T.; Houlihan, W. J., The Aldol Condensation. *Org. React.* **1968,** *16*, 1-438.

5. Zhang, G.; Hattori, H.; Tanabe, K., Aldol Condensation of Acetone/Acetone d6 over Magnesium Oxide and Lanthanum Oxide. *Appl. Catal.* **1988,** *40*, 183-190.

6. Shannon, I. R.; Lake, I. J. S.; Kemball, C., Catalytic Reactions on Titanium Dioxide. Part 2.-Exchange Reactions of Ketones with Deuterium Oxide and the Isomerization of n-Butenes. *Trans. Faraday Soc.* **1971,** *67*, 2760-2774.

7. Iglesia, E.; Barton, D. G.; Biscardi, J. A.; Gines, M. J. L.; Soled, S. L., Bifunctional Pathways in Catalysis by Solid Acids and Bases. *Catal. Today* **1997,** *38*, 339-360.

8. Barteau, M. A., Organic Reactions at Well-Defined Oxide Surfaces. *Chem. Rev.* **1996,** *96*, 1413-1430.

9. Idriss, H.; Diagne, C.; Hindermann, J. P.; Kiennemann, A.; Barteau, M. A., Reactions of Acetaldehyde on CeO_2 and CeO_2-Supported Catalysts. *J. Catal.* **1995,** *155*, 219-237.

10. Idriss, H.; Kim, K. S.; Barteau, M. A., Carbon-Carbon Bond Formation via Aldolization of Acetaldehyde on Single Crystal and Polycrystalline TiO_2 Surfaces. *J. Catal.* **1993,** *139*, 119-133.

11. Idriss, H.; Barteau, M. A., Selectivity and Mechanism Shifts in the Reactions of Acetaldehyde on Oxidized and Reduced TiO_2(001) Surfaces. *Catal. Lett.* **1996,** *40*, 147-153.

12. Canning, A. S.; Jackson, S. D.; McLeod, E.; Vass, E. M., Aldol Condensation of Acetone over CsOH/SiO_2: A Mechanistic Insight Using Isotopic Labelling. *Appl. Catal., A* **2005,** *289*, 59-65.

13. Griffiths, D. M.; Rochester, C. H., Infrared Study of the Adsorption of Acetone on Rutile. *J. Chem. Soc., Faraday Trans. 1* **1978,** *74*, 403-417.

14. Ai, M.; Fujihashi, H.; Hosoi, S.; Yoshida, A., Production of Methacrylic Acid by Vapor-Phase Aldol Condensation of Propionic Acid with Formaldehyde over Silica-Supported Metal Phosphate Catalysts. *Appl. Catal., A* **2003,** *252*, 185-191.

15. Zaki, M. I.; Hasan, M. A.; Pasupulety, L., Surface Reactions of Acetone on Al_2O_3, TiO_2, ZrO_2, and CeO_2: IR Spectroscopic Assessment of Impacts of the Surface Acid−Base Properties. *Langmuir* **2001,** *17*, 768-774.

16. Climent, M. J.; Corma, A.; Iborra, S.; Velty, A., Designing the Adequate Base Solid Catalyst with Lewis or Brønsted Basic Sites or with Acid–Base Pairs. *J. Mol. Catal. A: Chem.* **2002,** *182-183*, 327-342.

17. Snell, R. W.; Combs, E.; Shanks, B. H., Aldol Condensations Using Bio-Oil Model Compounds: The Role of Acid–Base Bi-Functionality. *Top. Catal.* **2010,** *53*, 1248-1253.

18. Seong, G.; Dejhosseini, M.; Adschiri, T., A Kinetic Study of Catalytic Hydrothermal Reactions of Acetaldehyde with Cubic CeO_2 Nanoparticles. *Appl. Catal., A* **2018,** *550*, 284-296.

19. Wan, M.; Liang, D.; Wang, L.; Zhang, X.; Yang, D.; Li, G., Cycloketone Condensation Catalyzed by Zirconia: Origin of Reactant Selectivity. *J. Catal.* **2018,** *361*, 186-192.

20. Kim, M.; Park, J.; Kannapu, H. P. R.; Suh, Y.-W., Cross-Aldol Condensation of Acetone and n-Butanol into Aliphatic Ketones over Supported Cu Catalysts on Ceria-Zirconia. *Catalysts* **2017,** *7*, 249.

21. Wang, S.; Goulas, K.; Iglesia, E., Condensation and Esterification Reactions of Alkanals, Alkanones, and Alkanols on TiO_2: Elementary Steps, Site Requirements, and Synergistic Effects of Bifunctional Strategies. *J. Catal.* **2016,** *340*, 302-320.

22. An, W., The Role of Synergic Interaction in Transition State Formation for the Aldol Reaction on a Metal Oxide Catalyst: A DFT Investigation. *Phys. Chem. Chem. Phys.* **2015,** *17*, 22529-22532.

23. Fan, D.; Dong, X.; Yu, Y.; Zhang, M., A DFT Study on the Aldol Condensation Reaction on MgO in the Process of Ethanol to 1,3-Butadiene: Understanding the Structure–Activity Relationship. *Phys. Chem. Chem. Phys.* **2017,** *19*, 25671-25682.

24. Chen, T. L.; Mullins, D. R., Adsorption and Reaction of Acetaldehyde over CeO_x(111) Thin Films. *J. Phys. Chem. C* **2011,** *115*, 3385-3392.

25. Mullins, D. R.; Albrecht, P. M., Acetaldehyde Adsorption and Reaction on CeO_2(100) Thin Films. *J. Phys. Chem. C* **2013,** *117*, 14692-14700.

26. Calaza, F. C.; Xu, Y.; Mullins, D. R.; Overbury, S. H., Oxygen Vacancy-Assisted Coupling and Enolization of Acetaldehyde on CeO_2(111). *J. Am. Chem. Soc.* **2012,** *134*, 18034-18045.

27. Mann, A. K. P.; Wu, Z.; Calaza, F. C.; Overbury, S. H., Adsorption and Reaction of Acetaldehyde on Shape-Controlled CeO_2 Nanocrystals: Elucidation of Structure–Function Relationships. *ACS Catal.* **2014,** *4*, 2437-2448.

28. Zhao, C.; Xu, Y., Simulated Temperature Programmed Desorption of Acetaldehyde on CeO_2(111): Evidence for the Role of Oxygen Vacancy and Hydrogen Transfer. *Top. Catal.* **2017,** *60*, 446-458.

29. Mullins, D. R.; Albrecht, P. M.; Calaza, F. C., Variations in Reactivity on Different Crystallographic Orientations of Cerium Oxide. *Top. Catal.* **2013,** *56*, 1345-1362.

30. Mullins, D. R.; Radulovic, P. V.; Overbury, S. H., Ordered Cerium Oxide Thin Films Grown on Ru(0001) and Ni(111). *Surf. Sci.* **1999,** *429*, 186-198.

31. Mullins, D. R.; Overbury, S. H.; Huntley, D. R., Electron Spectroscopy of Single Crystal and Polycrystalline Cerium Oxide Surfaces. *Surf. Sci.* **1998,** *409*, 307-319.

32. Stein, S. E., Mass Spectra. In *NIST Chemistry WebBook;* Linstrom, P. J., Mallard, W. G., Eds; NIST Standard Reference Database Number 69, National Institute of Standards and Technology: Gaithersburg, MD, http://webbook.nist.gov, (retrieved June 2018).

33. Ko, E. I.; Benziger, J. B.; Madix, R. J., Reactions of Methanol on W(100) and W(100)-(5×1)C Surfaces. *J. Catal.* **1980,** *62*, 264-274.

34. Kresse, G.; Furthmüller, J., Efficient Iterative Schemes for Ab Initio Total-Energy Calculations Using a Plane-Wave Basis Set. *Phys. Rev. B* **1996,** *54*, 11169-11186.

35. Perdew, J. P.; Chevary, J. A.; Vosko, S. H.; Jackson, K. A.; Pederson, M. R.; Singh, D. J.; Fiolhais, C., Atoms, Molecules, Solids, and Surfaces: Applications of the Generalized Gradient Approximation for Exchange and Correlation. *Phys. Rev. B* **1992,** *46*, 6671-6687.

36. Calaza, F. C.; Chen, T. L.; Mullins, D. R.; Xu, Y.; Overbury, S. H., Reactivity and Reaction Intermediates for Acetic Acid Adsorbed on CeO_2(111). *Catal. Today* **2015,** *253*, 65-76.

37. Klimeš, J.; Bowler, D. R.; Michaelides, A., Chemical Accuracy for the van der Waals Density Functional. *J. Phys.: Condens. Matter* **2010,** *22*, 022201.

38. Klimeš, J.; Bowler, D. R.; Michaelides, A., Van der Waals Density Functionals Applied to Solids. *Phys. Rev. B* **2011,** *83*, 195131.

39. Kresse, G.; Joubert, D., From Ultrasoft Pseudopotentials to the Projector Augmented-Wave Method. *Phys. Rev. B* **1999,** *59*, 1758-1775.

40. Dudarev, S. L.; Botton, G. A.; Savrasov, S. Y.; Humphreys, C. J.; Sutton, A. P., Electron-Energy-Loss Spectra and the Structural Stability of Nickel Oxide: An LSDA+U Study. *Phys. Rev. B* **1998,** *57*, 1505-1509.

41. Kresse, G.; Blaha, P.; Da Silva, J. L. F.; Ganduglia-Pirovano, M. V., Comment on "Taming Multiple Valency with Density Functionals: A Case Study of Defective Ceria". *Phys. Rev. B* **2005,** *72*, 237101.

42. Loschen, C.; Carrasco, J.; Neyman, K. M.; Illas, F., First-Principles LDA+U and GGA+U Study of Cerium Oxides: Dependence on the Effective U Parameter. *Phys. Rev. B* **2007,** *75*, 035115.

43. Lutfalla, S.; Shapovalov, V.; Bell, A. T., Calibration of the DFT/GGA+U Method for Determination of Reduction Energies for Transition and Rare Earth Metal Oxides of Ti, V, Mo, and Ce. *J. Chem. Theory Comput.* **2011,** *7*, 2218-2223.

44. Huang, M.; Fabris, S., CO Adsorption and Oxidation on Ceria Surfaces from DFT+U Calculations. *J. Phys. Chem. C* **2008,** *112*, 8643-8648.

45. Paier, J.; Penschke, C.; Sauer, J., Oxygen Defects and Surface Chemistry of Ceria: Quantum Chemical Studies Compared to Experiment. *Chem. Rev.* **2013,** *113*, 3949-3985.

46. Neugebauer, J.; Scheffler, M., Adsorbate-Substrate and Adsorbate-Adsorbate Interactions of Na and K Adlayers on Al(111). *Phys. Rev. B* **1992,** *46*, 16067-16080.

47. Henkelman, G.; Uberuaga, B. P.; Jónsson, H., A Climbing Image Nudged Elastic Band Method for Finding Saddle Points and Minimum Energy Paths. *J. Chem. Phys.* **2000,** *113*, 9901-9904.

48. Smidstrup, S.; Pedersen, A.; Stokbro, K.; Jónsson, H., Improved Initial Guess for Minimum Energy Path Calculations. *J. Chem. Phys.* **2014,** *140*, 214106.

49. Henkelman, G.; Jónsson, H., A Dimer Method for Finding Saddle Points on High Dimensional Potential Surfaces Using Only First Derivatives. *J. Chem. Phys.* **1999,** *111*, 7010-7022.

50. Heyden, A.; Bell, A. T.; Keil, F. J., Efficient Methods for Finding Transition States in Chemical Reactions: Comparison of Improved Dimer Method and Partitioned Rational Function Optimization Method. *J. Chem. Phys.* **2005,** *123*, 224101.

51. Monkhorst, H. J.; Pack, J. D., Special Points for Brillouin-Zone Integrations. *Phys. Rev. B* **1976,** *13*, 5188-5192.

52. Hensley, A. J. R.; Ghale, K.; Rieg, C.; Dang, T.; Anderst, E.; Studt, F.; Campbell, C. T.; McEwen, J.-S.; Xu, Y., DFT-Based Method for More Accurate Adsorption Energies: An Adaptive Sum of Energies from RPBE and vdW Density Functionals. *J. Phys. Chem. C* **2017,** *121*, 4937-4945.

53. Momma, K.; Izumi, F., VESTA: A Three-Dimensional Visualization System for Electronic and Structural Analysis. *J. Appl. Crystallogr.* **2008,** *41*, 653-658.

54. Esch, F.; Fabris, S.; Zhou, L.; Montini, T.; Africh, C.; Fornasiero, P.; Comelli, G.; Rosei, R., Electron Localization Determines Defect Formation on Ceria Substrates. *Science* **2005,** *309*, 752-755.

55. Torbrügge, S.; Reichling, M.; Ishiyama, A.; Morita, S.; Custance, Ó., Evidence of Subsurface Oxygen Vacancy Ordering on Reduced CeO_2(111). *Phys. Rev. Lett.* **2007,** *99*, 056101.

56. Kullgren, J.; Wolf, M. J.; Castleton, C. W. M.; Mitev, P.; Briels, W. J.; Hermansson, K., Oxygen Vacancies versus Fluorine at CeO_2(111): A Case of Mistaken Identity? *Phys. Rev. Lett.* **2014,** *112*, 156102.

57. Yang, Z.; Woo, T. K.; Baudin, M.; Hermansson, K., Atomic and Electronic Structure of Unreduced and Reduced CeO_2 Surfaces: A First-Principles Study. *J Chem. Phys.* **2004,** *120*, 7741-7749.

58. Fronzi, M.; Soon, A.; Delley, B.; Traversa, E.; Stampfl, C., Stability and Morphology of Cerium Oxide Surfaces in an Oxidizing Environment: A First-Principles Investigation. *J. Chem. Phys.* **2009,** *131*, 104701.

59. Ganduglia-Pirovano, M. V.; Da Silva, J. L. F.; Sauer, J., Density-Functional Calculations of the Structure of Near-Surface Oxygen Vacancies and Electron Localization on CeO_2(111). *Phys. Rev. Lett.* **2009,** *102*, 026101.

60. Murgida, G. E.; Ganduglia-Pirovano, M. V., Evidence for Subsurface Ordering of Oxygen Vacancies on the Reduced CeO_2(111) Surface Using Density-Functional and Statistical Calculations. *Phys. Rev. Lett.* **2013,** *110*, 246101.

61. Sutton, J. E.; Beste, A.; Overbury, S. H., Origins and Implications of the Ordering of Oxygen Vacancies and Localized Electrons on Partially Reduced CeO_2(111). *Phys. Rev. B* **2015,** *92*, 144105.

62. Conesa, J. C., Surface Anion Vacancies on Ceria: Quantum Modelling of Mutual Interactions and Oxygen Adsorption. *Catal. Today* **2009,** *143*, 315-325.

63. Hansen, H. A.; Wolverton, C., Kinetics and Thermodynamics of H_2O Dissociation on Reduced CeO_2(111). *J. Phys. Chem. C* **2014,** *118*, 27402-27414.

64. Li, H. Y.; Wang, H. F.; Guo, Y. L.; Lu, G. Z.; Hu, P., Exchange between Sub-Surface and Surface Oxygen Vacancies on CeO_2(111): A New Surface Diffusion Mechanism. *Chem. Comm.* **2011,** *47*, 6105-6107.

65. Fernández-Torre, D.; Carrasco, J.; Ganduglia-Pirovano, M. V.; Pérez, R., Hydrogen Activation, Diffusion, and Clustering on CeO_2(111): A DFT+U Study. *J. Chem. Phys.* **2014,** *141*, 014703.

TOC Graphic